14th International Symposium on Turbulence and Shear Flow Phenomena (TSFP14)
Heidelberg, Germany, July 28–31, 2026

DIRECT NUMERICAL SIMULATION OF HIGH-SPEED THREE-DIMENSIONAL LEADING EDGE BOUNDARY LAYER

Youcheng Xi
School of Aerospace Engineering
Tsinghua University
Beijing, China, 100084
xiyc@mail.tsinghua.edu.cn

Fu Song
School of Aerospace Engineering
Tsinghua University
Beijing, China, 100084
fs-dem@tsinghua.edu.cn

ABSTRACT

Direct numerical simulations (DNS) are performed to investigate the spatial evolution of a three-dimensional (3D) turbulent boundary layer over a swept blunt leading edge at a freestream Mach number of $M_\infty = 6.0$ and a unit Reynolds number of $Re_\infty = 1.8 \times 10^7 \mathrm{m}^{-1}$. This configuration induces a continuous transition from a quasi-two-dimensional state at the attachment line to a highly three-dimensional, non-equilibrium state downstream under the influence of strong geometry-induced pressure gradients. The simulation results reveal that while the flow at the attachment line exhibits characteristics of equilibrium turbulence satisfying classical scaling laws, the downstream acceleration leads to a significant phenomenon of "stress depletion." As the flow develops along the chordwise direction, the intense favorable pressure gradient (FPG) and crossflow shear disrupt the near-wall turbulence regeneration cycle. An analysis of the turbulent kinetic energy budget confirms that the production term is suppressed more rapidly than the dissipation term, eventually becoming insufficient to sustain turbulence, which provides definitive evidence of relaminarization process. Furthermore, spectral analysis indicates a scale-selective suppression where large-scale structures are annihilated, leaving only highly organized, streak-dominated fluctuations. Regarding thermal characteristics, the Strong Reynolds Analogy (SRA) relations between velocity and temperature fluctuations remain robust, indicating that thermal transport remains structurally locked to the surviving momentum streaks.

INTRODUCTION

Turbulent boundary layers are ubiquitous in various engineering applications, such as aerospace engineering, turbomachinery flows, and naval engineering. The vast majority of turbulent boundary layers encountered in practical engineering scenarios are three-dimensional (3D) and non-equilibrium. The three-dimensionality manifests as a misalignment between the primary flow direction and the pressure gradient (Schlichting & Gersten, 2017). This misalignment induces a crossflow velocity perpendicular to the primary flow direction, significantly altering the characteristics of the shear stress distribution within the boundary layer.

To advance our understanding of three-dimensional turbulent boundary layers, the primary requirement is access to high-fidelity data capable of characterizing their essential three-dimensional features. Such data can, in principle, be obtained through high-resolution experimental measurements or high-fidelity numerical simulations. However, accurately measuring the three-dimensional turbulent flow field within a boundary layer itself remains a challenge (Westerweel *et al.*, 2013).

In contrast, rapid advancements in computing power, particularly the advent of high-performance computing (HPC), have enabled the widespread application of direct numerical simulation (DNS) in turbulence research. However, the vast majority of existing DNS studies remain confined to statistically stationary, two-dimensional turbulent boundary layers, such as those over flat plates (Schlatter & Örlü, 2010; Pirozzoli & Bernardini, 2011) or in pipes (Yao *et al.*, 2023). Consequently, understanding how insights gained from canonical two-dimensional turbulent boundary layers can be extrapolated to genuinely three-dimensional scenarios is of paramount importance.

To better understand three-dimensional boundary layer flows and to simplify the problem, a commonly employed model is the infinity-swept configuration. In this configuration, although there exists a spanwise velocity component in the flow field, the primary variables are assumed to be functions of a planar coordinate only. As a result, this model is often referred to as a 2.5D model. However, such simulations inherently fail to accurately represent the realistic co-evolution of the primary flow and crossflow, along with their associated history effects.

Recently, we conducted high resolution simulations of the attachment-line boundary layer of a hypersonic swept blunt leading edge (Xi *et al.*, 2025). The swept blunt body configuration serves as a natural model to bridge two-dimensional and three-dimensional turbulent boundary layers. Unlike temporal simulations that rely on artificial initial conditions, this configuration offers a continuous spatial evolution: from a quasi-two-dimensional flow at the attachment line to a highly three-dimensional, non-equilibrium state downstream. This allows for a precise interrogation of how 3D turbulence structures evolve spatially under realistic, geometry-induced pressure gradients.

Motivated by the aforementioned challenges, there is a critical need to establish a physically realistic and high-fidelity benchmark database for three-dimensional non-equilibrium turbulent boundary layers through high-resolution numerical simulation. Consequently, a fundamental objective of this work is to leverage high-resolution DNS for three-dimensional turbulent boundary layers and construct an engineering-relevant database characterizing three-dimensional non-equilibrium turbulent boundary layer physics.

Therefore, in this study, leveraging insights gained from prior high-resolution implicit LES (Xi *et al.*, 2025), we conduct DNS within the fully developed turbulent region to address these gaps. We employ a realistic swept blunt leading edge, a configuration that intrinsically embodies the spatial coupling between geometry-induced pressure gradients, crossflow shear, and turbulence history effect. The remainder of this paper is structured as follows: Section 2 provides a detailed discussion of the methodology, including governing equations, numerical methods, and computational setup. Fundamental computational results concerning mean flow properties and turbulence statistics are presented and discussed in Section 3. Finally, concluding remarks are provided in Section 4.

METHODOLOGY

Governing Equations and Numerical Methods

The governing equations for all simulations in this work are the dimensionless compressible Navier–Stokes equations for a Newtonian fluid. The equations are solved using a high-order finite difference code developed at Tsinghua University. A shock-fitting method is used to compute steady hypersonic viscous flow together with high-order accurate non-compact finite differences methods. The 5th-order upwind scheme (for inviscid flux) and the 6th-order centre scheme (for viscous flux) are used to compute the flow field. A 4th-order Runge-Kutta method is applied for the time integration, and the simulations are performed until the maximum residual reaches a small value on the order of 10^{-15}.

For three-dimensional calculations presented in this study, a hybrid high-order finite difference scheme, including the seventh-order upwind scheme, fifth-order and seventh-order WENO schemes (Jiang & Shu, 1996), together with a shock sensor (Dang *et al.*, 2022), is used for the inviscid flux in the characteristic form. Based on that formulation, during the calculation, more than 98% of the regions use the linear seventh-order upwind scheme, only a few regions corresponding to discontinuities use the nonlinear WENO schemes, which greatly increases the calculation efficiency. A standard sixth-order central difference scheme is used for viscous flux. Time advancement is achieved by the explicit third-order total variation diminishing Runge-Kutta scheme.

Computational Model and Setup

Our computational model is designed based on an experimental configuration (see Xi *et al.* (2025) for more details). The model is the front part of a delta wing with a swept angle Λ of 45 degrees. The thickness of the wing is $2L_4 = 40$. The computational model can be likened to a sandwich-like configuration, where the top and bottom layers consist of semicircles

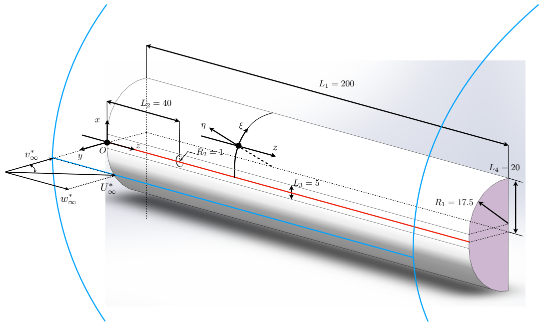

Figure 1: Schematics of the swept blunt leading edge used for numerical simulations. The blue lines stand for the leading shock and the red line represents the leading edge attachment line.

with a radius of $R_1 = 17.5$, and the intermediate layer is a flat rectangular slab with a width of $L_3 = 5$. Together, these three layers form the complete swept blunt body configuration.

The roughness element is located at $z = L_2 = 40$, at the center of the leading flat rectangular slab. The radius of the roughness is $R_2 = 1$. The length of the whole model is designed as $L_1 = 200$. Based on experiments, the surface temperature is set to $T^*_w = 370$K, with freestream Mach number $M_\infty = 6.0$, unit Reynolds number $Re_\infty = 1.8 \times 10^4$, and freestream temperature $T^*_\infty = 56.58$K.

The calculation process for this problem is divided into four steps: (1) two-dimensional calculation with infinity span assumption using shock-fitting solver; (2) three-dimensional pre-calculation with periodic boundary condition along the spanwise direction; (3) fully three-dimensional calculation; (4) extraction of a computational domain for DNS with refined grid meeting DNS requirements.

Grid Resolution and Validation

The computational grid for the present DNS is designed according to the following principles, extending classical flat-plate boundary layer DNS standards to address the unique complexities of three-dimensional turbulent boundary layers. The grid numbers used for DNS of the selected region are $N_\xi \times N_\eta \times N_z = 4801 \times 601 \times 2001$.

Throughout the entire three-dimensional boundary layer, the grid spacings ($\Delta\xi^+$, $\Delta\eta^+$, Δz^+), based on inner scales, in all coordinate directions remain below 4.5. The grid spacings normalized by the local Kolmogorov length scale $\eta_k = \left(\nu^3/\varepsilon\right)^{1/4}$ are always smaller than $4\eta_K$ inside the present three-dimensional turbulent boundary layer. Furthermore, the effective mesh spacing, Δ^+, ranges between 2 and 4 across the entire boundary layer. These grid-resolution metrics demonstrate that the predominant scales of the turbulent motion inside the three-dimensional turbulent boundary layer can be adequately resolved.

Statistical convergence is verified by calculating the averages of the components in the transport equations of Reynolds stresses over two different numbers of snapshots. The basic numbers of snapshots are chosen as $T_s = 62.5\delta_b/\bar{u}_{\tau,m}$ ($\sim 2000\delta_b/U^*_\infty$), where $\bar{u}_{\tau,m}$ is the maximum friction velocity for the present three-dimensional boundary layer.

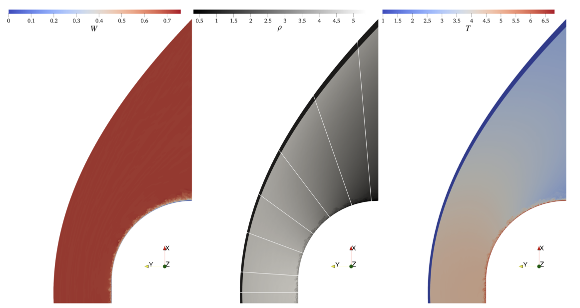

Figure 2: Instantaneous spanwise velocity w, density ρ and temperature T distributions in the $x-y$ plane. Seven chordwise locations ξ_i are marked from the exact attachment line to the chordwise exit.

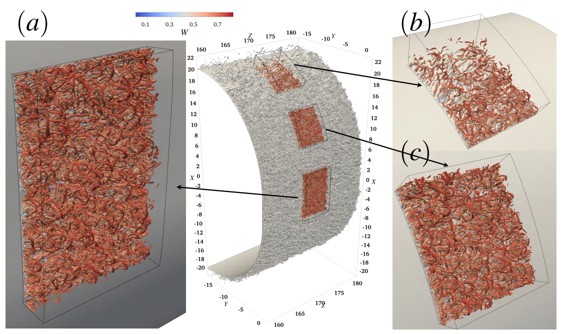

Figure 3: Snapshots of vortices by iso-surfaces of the λ_2-criterion with $\lambda_2 = -0.35$. The colour stands for the spanwise velocity component W.

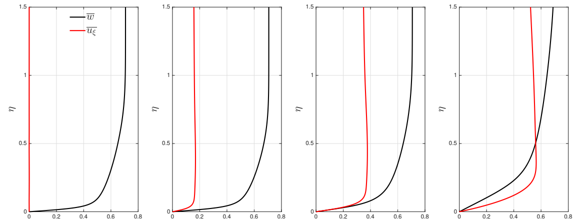

Figure 4: Schematic of spanwise velocity profiles $\overline{w}$ and chordwise velocity profiles $\overline{u_\xi}$ at chordwise positions ξ_1, ξ_3, ξ_5, and ξ_7.

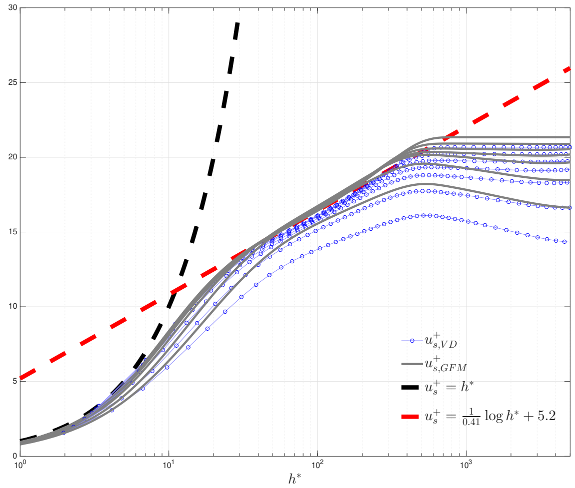

Figure 5: Streamwise mean-velocity profiles, transformed according to VD and GFM transformations, at chordwise positions $\xi_1, \xi_2, \cdots, \xi_7$. All the scales and variables are scaled based on $\overline{\tau}_w$, total wall-shear stress.

RESULTS AND DISCUSSION

General Flow Features

Figure 2 shows instantaneous spanwise velocity, density, and temperature features on an $x-y$ cross-section. As the flow field is statistically symmetric about the attachment-line plane, the results begin from a point slightly below the attachment-line plane and extend to the upper chordwise outlet. It can be clearly observed that as the flow develops from the attachment-line region toward the chordwise outlet, the thickness of the turbulent boundary layer progressively increases, while the fluid density within the boundary layer gradually decreases.

To provide a more intuitive understanding of the turbulent flow field, the instantaneous vortical structures within the complete computational domain are visualized using iso-surfaces of the λ_2-criterion, as shown in figure 3. The vortical structures in the attachment-line region remain similar to those in a conventional two-dimensional turbulent boundary layer over a flat plate, with no pronounced tilting or skewing observed. In the downstream chordwise regions, however, as the flow accelerates, the vortices exhibit significant skewing due to the crossflow/pressure gradient induced by the geometry. Due to the strong favorable pressure gradient from the attachment line to the chordwise outlet, the vortical structures are observed to gradually become more sparse, indicating a local reduction in turbulence intensity.

Mean Flow Statistics and Crossflow Development

Figure 4 presents the variation of mean velocity profiles at different chordwise stations, while the corresponding three-dimensional velocity changes are illustrated. From the figures, it can be clearly observed that, with the change in chordwise station, the fluid accelerates gradually along the $\xi-$direction under the influence of the chordwise pressure gradient. At some downstream stations, a distinct velocity overshoot appears, where the velocity magnitude within the boundary layer exceeds the potential flow velocity at the boundary layer edge. As the $\xi-$direction velocity increases, the corresponding flow deflection angle of the three-dimensional boundary layer also becomes larger, and the magnitude of the crossflow velocity gradually increases.

To better examine the fundamental characteristics of the mean flow, we check whether the corresponding mean velocity satisfies the classical velocity scaling or the law of the wall. The transformed streamwise velocity profiles are presented in Figure 5, ranging from position ξ_1 (the exact attachment line) to the downstream chordwise position ξ_7. It can be clearly observed that the GFM transformation collapses the corresponding velocity profiles in the logarithmic region better than the classic Van Driest transformation. Additionally, two noteworthy points arise. First, the velocity profiles in the region from the buffer layer to the viscous sublayer do not collapse well. A possible reason for this is that as the boundary layer flow develops three-dimensionally, the shear introduced by the crossflow velocity gradually increases, making the scaling based solely on the total wall shear stress τ_w less appropriate.

Another noteworthy characteristic of the mean flow is the relationship between the mean temperature and the mean velocity. This relationship reflects the intrinsic connection

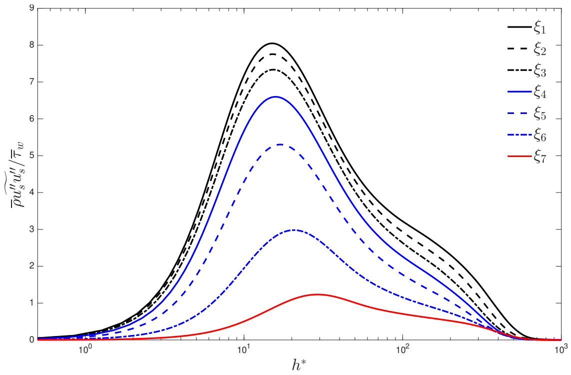

Figure 6: Reynolds stress profiles at several ξ locations. $\overline{\rho}\widetilde{u_s''u_s''}/\overline{\tau}_w$ shows dramatic suppression from ξ_1 to ξ_7.

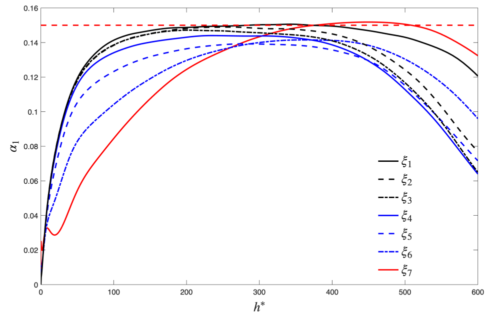

Figure 7: Surface normal profiles of the turbulent structure parameter α_1 at several locations along ξ as a function of wall-normal distance h^*.

between kinetic energy and internal energy. The mean temperature-velocity relation model given by Zhang *et al.* (2014), which is also known as the generalized reynolds analogy (GRA), shows good agreement with the DNS results, with only slight deviations appearing in the region near the boundary layer edge.

Turbulence Statistics and Stress Depletion

Figure 6 presents the wall-normal profiles of the Reynolds stress tensor components, scaled by the local wall shear stress $\overline{\tau}_w$, in the local streamline coordinate system. This transformation allows for a direct physical interpretation of the turbulence evolution from the attachment line (ξ_1) to the chordwise downstream (ξ_7). Three distinctive features regarding the interplay between three-dimensionality and the strong favorable pressure gradient (FPG) are identified.

First, a dramatic suppression of turbulence intensity, referred to as stress depletion, is observed in the streamwise components. At the attachment line (ξ_1), the profiles of the streamwise normal stress $\overline{\rho u_s'' u_s''}$ and the primary shear stress $\overline{\rho u_s'' u_\eta''}$ exhibit typical characteristics of fully developed turbulence, resembling canonical two-dimensional distributions. However, as the flow accelerates downstream ($\xi_1 \rightarrow \xi_7$), the magnitude of these stresses decreases monotonically and significantly. By the chordwise exit (ξ_7), the primary shear stress $\overline{\rho u_s'' u_\eta''}$ has nearly vanished. This behavior indicates a strong tendency towards relaminarization, driven by the intense acceleration (velocity overshoot) and the associated strong favorable pressure gradient, which inhibits turbulence production and stretches fluid elements.

Second, the crossflow-related stresses exhibit a non-monotonic evolution due to the competing mechanisms of three-dimensional shear and flow acceleration. At the attachment line (ξ_1), the crossflow components are negligible, consistent with the statistical symmetry of the flow. In the intermediate region ($\xi_2 \rightarrow \xi_5$), these components rise sharply, reflecting the establishment of the three-dimensional boundary layer and the generation of turbulence via crossflow shear. However, in the downstream region ($\xi_6 \rightarrow \xi_7$), the stabilizing effect of the FPG becomes dominant, overwhelming the production due to crossflow shear. Consequently, the crossflow Reynolds stresses collapse alongside the streamwise components, despite the flow being highly three-dimensional.

Third, a distinct outward shift of the Reynolds stress peaks is observed. The location of the peak stress (h^*) moves progressively away from the wall as the flow evolves from $\xi_1 \rightarrow \xi_7$. This phenomenon highlights significant turbulence history effects: the near-wall turbulence responds rapidly to the local acceleration and is suppressed effectively, whereas the large-scale structures in the outer layer exhibit a "memory" of the upstream turbulence and decay more slowly. This decoupling between the inner and outer layers suggests that local equilibrium assumptions (and simple eddy-viscosity models) may fail to capture the physics in this strongly accelerated, three-dimensional regime.

To further elucidate the mechanism underlying the observed stress depletion, we examine the Townsend structural parameter, α_1 defined as

$$\alpha_1 = \frac{\sqrt{\widetilde{u_\xi'' u_\eta''}^2 + \widetilde{u_\eta'' w''}^2}}{2k}, \tag{1}$$

where k is the turbulent kinetic energy. Figure 7 illustrates the wall-normal profiles of α_1 at various chordwise locations. The deviation from the equilibrium value of 0.15 provides compelling evidence of the structural distortion within the three-dimensional boundary layer. Specifically, in the downstream region, a precipitous drop in α_1 is observed throughout the bulk of the boundary layer, with values falling significantly below 0.15. This collapse of structural efficiency confirms that the reduction in Reynolds stress discussed previously is not merely a consequence of reduced turbulent kinetic energy, but rather stems from a fundamental decorrelation between velocity fluctuations.

Mechanism of Relaminarization

The turbulent kinetic energy equation provides a definitive mechanistic explanation for the observed flow relaminarization. Figure 8 illustrates the wall-normal profiles of the ratio between the production term (P_k^+) and the viscous dissipation term ($\phi_{\varepsilon_k}^+$), plotted as $P_k^+/\phi_{\varepsilon_k}^+ - 1$.

At the attachment line (ξ_1), the profile exhibits a canonical distribution typical of equilibrium turbulent boundary layers, with a distinct peak reaching approximately 1.0 within the buffer layer ($h^* \approx 15$). This indicates that the production of turbulent kinetic energy significantly exceeds dissipation ($P_k^+ \approx 2\phi_{\varepsilon_k}^+$), sustaining the turbulence regeneration cycle and energy transport to the outer layer.

However, a dramatic collapse of this energy balance is observed as the flow accelerates downstream. The peak value of the ratio decreases monotonically from ξ_1 to ξ_7. Strikingly, at the chordwise exit (ξ_7), the ratio drops below zero across the

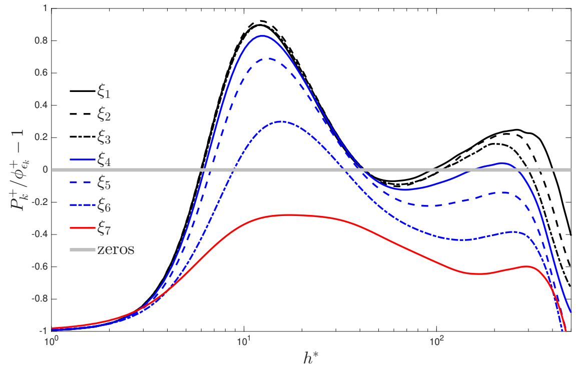

Figure 8: Balance of production and dissipation of turbulent kinetic energy at several ξ. The ratio $P_k^+/\phi_{\varepsilon_k}^+ - 1$ drops below zero at ξ_7, indicating relaminarization.

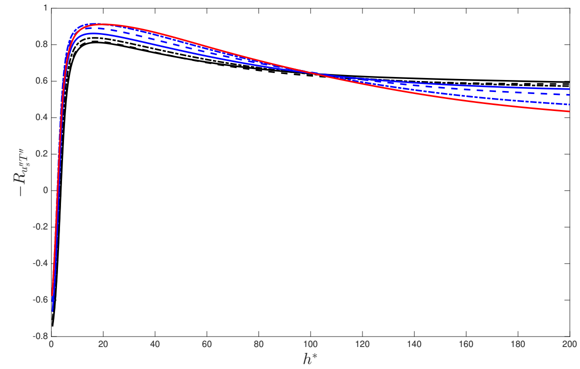

Figure 9: Temperature-velocity correlation coefficients. The streamwise correlation $-R_{u_s''T''}$ remains near -0.8 from ξ_1 to ξ_7, proving robust thermal-momentum coupling.

entire boundary layer, including the buffer region. Physically, this condition ($P_k^+ < \phi_{\varepsilon_k}^+$) implies that the local extraction of energy from the mean flow by Reynolds stresses is insufficient to overcome viscous dissipation. The further drop below zero implies that turbulent production is insufficient to balance dissipation, leading to a decay in turbulent kinetic energy.

This global deficit in turbulent kinetic energy production confirms that the strong favorable pressure gradient and the associated flow acceleration have disrupted the near-wall bursting events. Consequently, the turbulence is no longer self-sustaining, leading to the relentless decay of turbulent fluctuations and confirming the occurrence of relaminarization in the downstream region.

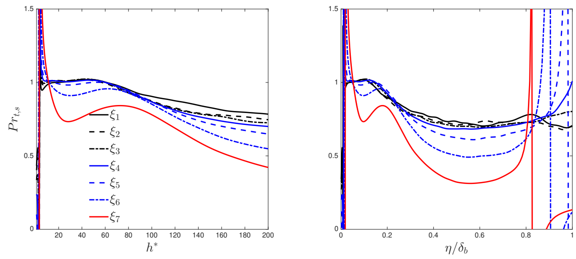

Figure 10: Turbulent Prandtl number $Pr_{t,s}$. The significant drop below 1 in the outer layer at downstream stations (ξ_5, ξ_7) indicates momentum transport is suppressed faster than heat transport under strong acceleration.

Compressibility Effects and Thermal Characteristics

Given the high freestream Mach number and the cold wall boundary condition, assessing the validity of Morkovin's hypothesis (Morkovin, 1962) is crucial. This hypothesis postulates that the turbulent structure of a compressible boundary layer remains similar to that of an incompressible one, provided that local variations in fluid properties are accounted for.

We first examine the validity of Morkovin's scaling for the Reynolds stress magnitudes. At the attachment line (ξ_1), the profile collapses excellently with incompressible data, confirming that at the attachment line, the turbulence is in a state of quasi-equilibrium where Morkovin's scaling holds valid. However, a dramatic departure is observed downstream ($\xi_3 \to \xi_7$), where the peak stress intensity drops by nearly 90%. This failure of scaling is not due to a breakdown of the compressibility transformation itself, but is a consequence of relaminarization driven by the strong acceleration, which disrupts the turbulence regeneration cycle.

To understand the thermal-kinematic coupling, we examine two key diagnostics: the temperature-velocity correlation coefficients $R_{u''T''}$ and the turbulent Prandtl number Pr_t. Figure 9 presents the correlation coefficients between temperature fluctuations and various velocity components. A striking observation is the consistently high negative correlation (around -0.8) between streamwise velocity and temperature fluctuations ($-R_{u_s''T''}$) across all chordwise stations, including the highly relaminarized downstream region (ξ_7). This demonstrates that the thermal field remains tightly locked to the streamwise momentum streaks, even as turbulence intensity collapses. In contrast, correlations involving crossflow velocity components ($-R_{u_c''T''}$) are significantly weaker, confirming that heat is primarily transported along, rather than across, the surviving streamwise-oriented structures.

Figure 10 shows the turbulent Prandtl number $Pr_{t,s}$, which quantifies the relative efficiency of momentum vs. heat transport. At the attachment line (ξ_1), $Pr_{t,s}$ exhibits a canonical plateau around 1 in the log region. However, a profound non-equilibrium effect emerges downstream: $Pr_{t,s}$ drops significantly below 1 in the outer layer, reaching values as low as 0.4 at ξ_7. This reduction indicates that momentum transport (Reynolds shear stress) is suppressed by the favorable pressure gradient more rapidly than thermal transport (turbulent heat flux). The thermal field exhibits a stronger 'history effect', maintaining coherent transport structures slightly longer than the momentum field. Nevertheless, $Pr_{t,s}$ remains positive and bounded, confirming that the fundamental coupled transport mechanism persists even during relaminarization.

These thermal diagnostics collectively provide strong evidence for the persistence of the Strong Reynolds Analogy (SRA) in a structural sense. While the turbulence intensity decays dramatically, the *structural relationship* between velocity and temperature fluctuations remains intact. The thermal field behaves as a passive scalar faithfully advected by the surviving streamwise streaks, leading to thermal relaminarization that mirrors the momentum relaminarization. This finding underscores the robustness of SRA-like relationships even in highly non-equilibrium, three-dimensional, and relaminarizing flows.

CONCLUSIONS

In this study, high-fidelity direct numerical simulations were conducted to characterize the physics of a spatially developing three-dimensional turbulent boundary layer over a hypersonic swept blunt leading edge, within a unified and self-consistent framework, the interplay of geometry-induced pressure gradients, crossflow shear, and the spatial history effects of turbulence. The simulation covers the continuous evolution from the attachment line to the downstream chordwise exit, providing a unique database for analyzing geometry-induced non-equilibrium effects. The main conclusions are summarized as follows:

1. **Mean Flow and Crossflow Development:** The flow field exhibits strong three-dimensionality driven by the swept geometry. While the attachment line flow behaves similarly to a canonical two-dimensional turbulent boundary layer, the downstream flow undergoes rapid acceleration, resulting in a distinct velocity overshoot and a substantial crossflow velocity component. The boundary layer is subjected to a strong favorable pressure gradient (FPG) primarily acting in the crossflow direction.
2. **Stress Depletion and Non-equilibrium Statistics:** A severe suppression of turbulence intensity, known as stress depletion, is observed as the flow accelerates downstream. The Reynolds stress profiles show that the turbulent shear stress decays significantly, and the structural parameter α_1 drops well below the equilibrium value of 0.15.
3. **Mechanism of Relaminarization:** The budget analysis of turbulent kinetic energy identifies the physical mechanism governing the flow evolution. At the attachment line, the production of turbulence balances dissipation. However, in the downstream region, the strong FPG and flow acceleration inhibit the bursting events, causing the production term P_k to collapse faster than the viscous dissipation ε. The appearance of a global energy deficit ($P_k < \varepsilon$) across the boundary layer confirms that the flow undergoes a tendency towards relaminarization in the downstream region.
4. **Compressibility Effects and Strong Reynolds Analogy:** The compressibility transformations and Morkovin's hypothesis, which work well at the attachment line, fail to collapse the Reynolds stress profiles in the downstream region. This failure is attributed to the intrinsic disruption of the turbulence structure by relaminarization rather than compressibility effects alone. Nevertheless, the velocity-temperature correlations remain high, and the thermal field maintains a strong structural similarity to the momentum field, adhering to the physical essence of the Strong Reynolds Analogy (SRA) even in this highly non-equilibrium regime.

The present study underscores the limitation of equilibrium turbulence assumptions in predicting flows over realistic hypersonic vehicles. The detailed dataset provided herein serves as a valuable benchmark for the development of advanced turbulence models capable of capturing history effects, strong acceleration, and relaminarization in three-dimensional boundary layers.

ACKNOWLEDGMENTS

This work received support from the NSFC Grants 12388101, U2541235, 12202242 and 12172195. We acknowledge Yancheng MetaStone Tech. Co. for providing us with the computational resources required by this work. The authors also acknowledge the computational resources provided by the Yancheng Supercomputing Center under project number 20231001.

REFERENCES

Dang, Guanlin, Liu, Shiwei, Guo, Tongbiao, Duan, Junyi & Li, Xinliang 2022 Direct numerical simulation of compressible turbulence accelerated by graphics processing unit: An open-source high accuracy accelerated computational fluid dynamic software. *Physics of Fluids* **34** (12), 126106.

Jiang, G. S. & Shu, C. W. 1996 Efficient implementation of weighted eno schemes. *Journal of Computational Physics* **126** (1), 202–228.

Morkovin, M. V. 1962 Effects of compressibility on turbulent flows. *In Mecanique de la Turbulence (ed. A. Favre)* p. 367–380.

Pirozzoli, Sergio & Bernardini, Matteo 2011 Turbulence in supersonic boundary layers at moderate reynolds number. *Journal of Fluid Mechanics* **688**, 120–168.

Schlatter, Philipp & Örlü, Ramis 2010 Assessment of direct numerical simulation data of turbulent boundary layers. *Journal of Fluid Mechanics* **659**, 116–126.

Schlichting, Hermann & Gersten, Klaus 2017 *Boundary-Layer Theory*, 9th edn. Berlin Heidelberg: Springer-Verlag Berlin Heidelberg.

Westerweel, Jerry, Elsinga, Gerrit E. & Adrian, Ronald J. 2013 Particle image velocimetry for complex and turbulent flows. *Annual Review of Fluid Mechanics* **45** (Volume 45, 2013), 409–436.

Xi, Youcheng, Yan, Bowen, Yang, Guangwen, Sha, Xinguo, Zhu, Dehua & Fu, Song 2025 Numerical simulations of attachment-line boundary layer in hypersonic flow. part 1. roughness-induced subcritical transitions. *Journal of Fluid Mechanics* **1009**, A63.

Yao, Jie, Rezaeiravesh, Saleh, Schlatter, Philipp & Hussain, Fazle 2023 Direct numerical simulations of turbulent pipe flow up to $re_\tau \approx 5200$. *Journal of Fluid Mechanics* **956**, A18.

Zhang, You-Sheng, Bi, Wei-Tao, Hussain, Fazle & She, Zhen-Su 2014 A generalized reynolds analogy for compressible wall-bounded turbulent flows. *Journal of Fluid Mechanics* **739**, 392–420.